Ultrathin, High-Aspect Ratio, and Free-Standing Magnetic Nanowires by Exfoliation of Ferromagnetic Quasi-One-Dimensional van der Waals Lattices

Ultrathin, High-Aspect Ratio, and Free-Standing Magnetic Nanowires by Exfoliation of Ferromagnetic Quasi-One Dimensional van der Waals Lattices

Yi Qu,[a,+] Maxx Q. Arguilla,[a,+] Qiang Zhang,[b] Xin He,[a] and Mircea Dincă[a,*]

[a]Department of Chemistry, Massachusetts Institute of Technology, Cambridge, Massachusetts 02139, USA

[b]Neutron Scattering Division, Oak Ridge National Laboratory, Oak Ridge, Tennessee 37831, USA

ABSTRACT: Driven by numerous discoveries of novel physical properties and integration into functional devices, interest in one-dimensional (1D) magnetic nanostructures has grown tremendously. Traditionally, such structures are accessed with bottom-up techniques, but these require increasing sophistication to allow precise control over crystallinity, branching, aspect-ratio, and surface termination, especially when approaching the sub-nanometer regime in magnetic phases. Here, we show that mechanical exfoliation of bulk quasi-one-dimensional crystals, a method similar to those popularized for two-dimensional van der Waals (vdW) lattices, serves as an efficient top-down method to produce ultrathin freestanding nanowires that are both magnetic and semiconducting. We use $CrSbSe_3$ as a representative quasi-1D van der Waals crystal with strong magnetocrystalline anisotropy, and show that it can be exfoliated into nanowires with average cross-section of 10 ± 2.8 nm. The $CrSbSe_3$ nanowires display reduced Curie-Weiss temperature, but higher coercivity and remanence than the bulk phase. The methodology developed here for $CrSbSe_3$, a representative for a vast class of 1D vdW lattices, serves as a blueprint for investigating confinement effects for 1D materials and accessing functional nanowires that are difficult to produce *via* traditional bottom-up methods.

INTRODUCTION

Nanoscale low-dimensional magnetic devices have enabled studies of a vast range of exotic physical phenomena[1-3] such as spin-Peierls transitions in spin chains[4] and superconductivity in spin-ladder systems, [5] and have given rise to technologies spanning magnetic refrigeration,[6-7] implantable bioelectronics,[8-9] and data storage devices.[10-14] Many of these technologies benefit from the use of one-dimensional (1D) magnetic nanostructures, which have smaller footprints, greater sensitivity towards external stimuli, and enhanced coercivity enabled by their inherent shape anisotropy.[15] The advantages conferred by nanowires have led to numerous advances in bottom-up synthetic routes, such as vapor- and solution-phase growth,[16-18] electrodeposition,[19-21] and lithographic methods,[22-23] which can yield freestanding magnetic nanowires with well-defined diameters, lengths, compositions, and phase purity. Challenges remain, however, because these traditional bottom-up methods often do not allow for precise control over the long-range nanowire morphologies, and they typically lead to surface passivation and the formation of defects.[24-29] Alternatively, one can employ top-down approaches to isolate wires from bulk crystals, as demonstrated with $Mo_6S_3I_6$,[30-33], SnIP,[34] and V_2Se_9,[35-36] which comprise strong covalently-bonded molecular chains connected by van der Waals (vdW) inter-chain interactions. This approach has shown great promise because starting from ostensibly more highly ordered and surface defect-free bulk crystals yields nanowires whose structural and physical properties enable potential applications in transistors and photovoltaic devices.[30, 37-47] To our knowledge, however, these softer methodologies have not been extended to magnetic vdW phases and, critically, their utility in accessing highly desirable ultrathin magnetic nanowires remains largely unexplored.

Here, we describe a top-down approach to fabricating semiconducting magnetic nanowires from bulk crystals comprised of one-dimensional inorganic magnetic chains held together predominantly by vdW interactions. Contrasting with related methods pioneered for instance with the solution stabilization of $Li_2Mo_6Se_6$ highly polar solvents,[48-49] this method is distinct because it does not require cation solvation and produces free-standing nanowires that do not require solution or surface stabilization. In fact, the methodology reported here is most closely related to the mechanical exfoliation of 2D vdW phases popularized with graphene and transition metal dichalcogenides. Indeed, although exfoliation is obviously widely used with bulk 2D vdW lattices, including for producing free-standing ultrathin magnetic sheets,[50-57] it has rarely, if ever, been used on bulk 1D vdW magnetic lattices, whose magnetic behavior upon dimensional reduction to the nanowire regime likewise remains poorly understood.

To highlight the potential utility of 1D vdW exfoliation in the production of magnetic nanowires, we chose $CrSbSe_3$ as a representative example. Although there are numerous bulk phases that can be described as 1D vdW crystals, exceedingly few show magnetic ordering.[58-62] Featuring weakly associated double-rutile chains of covalently bonded atoms, bulk $CrSbSe_3$ exhibits robust ferromagnetic ordering below 71 K. [63-64] The Sb atoms are critical: their lone pairs provide steric repulsion that separate individual $CrSbSe_3$ chains and open vdW gaps. We used time-of-flight (T.O.F.) powder neutron diffraction to establish the ferromagnetic ground state and the apparent magnetocrystalline anisotropy of $CrSbSe_3$ and show that as-synthesized $CrSbSe_3$ crystals can be readily exfoliated into 10 ± 2.8 nm thick nanowires. Importantly, the exfoliated $CrSbSe_3$ nanowires are resistant to oxidation under ambient conditions. Exfoliation of the bulk crystals into long and thin nanowires significantly decreases the Curie-Weiss temperature (θ_{CW}) and simultaneously increases their coercivity and remanence. Exfoliation thus produces a harder ferromagnetic phase than bulk $CrSbSe_3$, as has also been seen upon nanostructuring traditional ferromagnets such as Ni and Fe_2O_3.[65-66] These findings demonstrate that well-established exfoliation methods can be adapted to new classes of functional vdW lattices, particularly for the creation of 1D magnetic nanostructures.

RESULTS AND DISCUSSTION

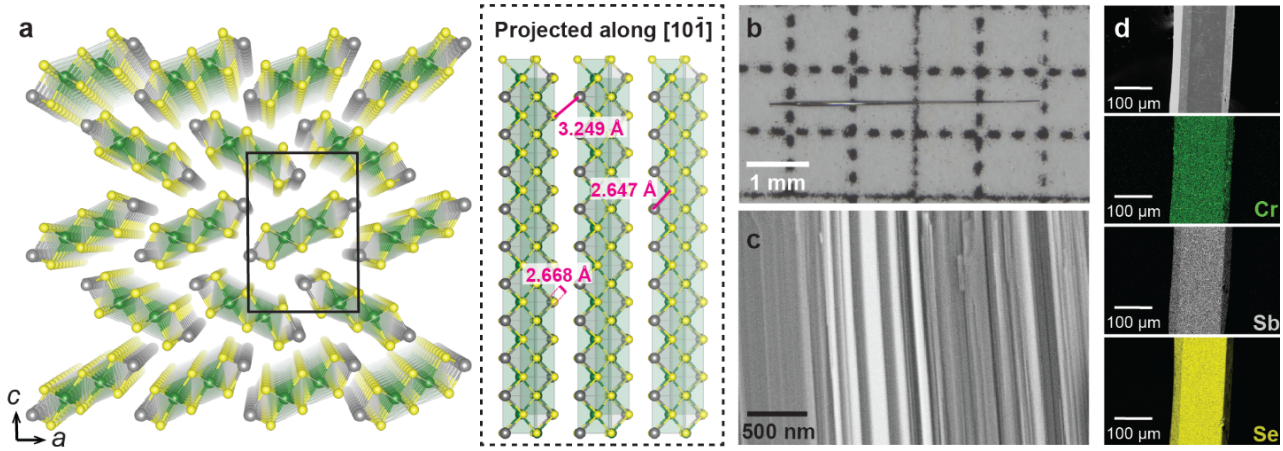

Figure 1. Structure and characterization of $CrSbSe_3$. a) X-ray crystal structure of $CrSbSe_3$ at 298 K, with the unit cell outlined in black (left) and the double-rutile chains extending along the ***b*** axis labeled with three relevant of Sb-Se distances (right). Green, grey and yellow spheres represent Cr, Sb, and Se, respectively. **b)** A single crystal of flux-grown $CrSbSe_3$. **c)** SEM micrograph of an as-synthesized $CrSbSe_3$ single crystal after mechanical cleavage. **d)** SEM micrograph with the corresponding EDS elemental maps of $CrSbSe_3$.

As reported previously, $CrSbSe_3$ crystallizes in the orthorhombic *Pnma* space group and features double-rutile chains of covalently bonded atoms extending along the *b* axis (**Figure 1a**).[63-64] The Sb atoms occupying the edge of the double-rutile chains bind three Se atoms in trigonal pyramidal geometry. Owing to the close electronegativity values of Sb and Se, the lone pair on Sb provides steric repulsion and forms a vdW gap with Se orbitals on neighboring chains. Indeed, the nearest neighbor distance between a Sb atom on one chain and a Se atom on an adjacent chain, 3.2494(9) Å, is much longer than the Sb–Se bond distances within a chain: 2.6473(8) Å and 2.6679(11) Å (**Figure 1a, Table S4**). Bulk $CrSbSe_3$ is grown either by typical solid state melt synthesis, which yields polycrystalline powders, or by flux growth, which yields needle-like millimeter-sized single crystals with fibrous morphology, a macroscopic indication of the quasi-1D vdW nature of the crystals (**Figure 1b,c,** see **Section I** in **Supporting Information** for synthesis details). Elemental mapping by energy-dispersive X-ray spectroscopy (EDS) confirmed the homogeneous distribution of Cr, Sb, and Se throughout the crystals (**Figure 1d**).

We used T.O.F. powder neutron diffraction to determine the magnetic structure and correlate structural parameters in $CrSbSe_3$ with its established bulk ferromagnetic behavior. It had been shown that the ferromagnetic transition temperature (T_C) of bulk $CrSbSe_3$ is at approximately 71 K. As such, we refined neutron diffraction data above and below T_C. Significantly, data collected at 10 K displayed increased intensity for several Bragg peaks at the high T.O.F. (> 100,000 µsec) or *d*-spacing region (**Figure 2a**). Indexing and refinement of this data revealed that the magnetic unit cell has the same parameters as the crystallographic unit cell (**Figure 2b, Table S2, S3**). Rietveld

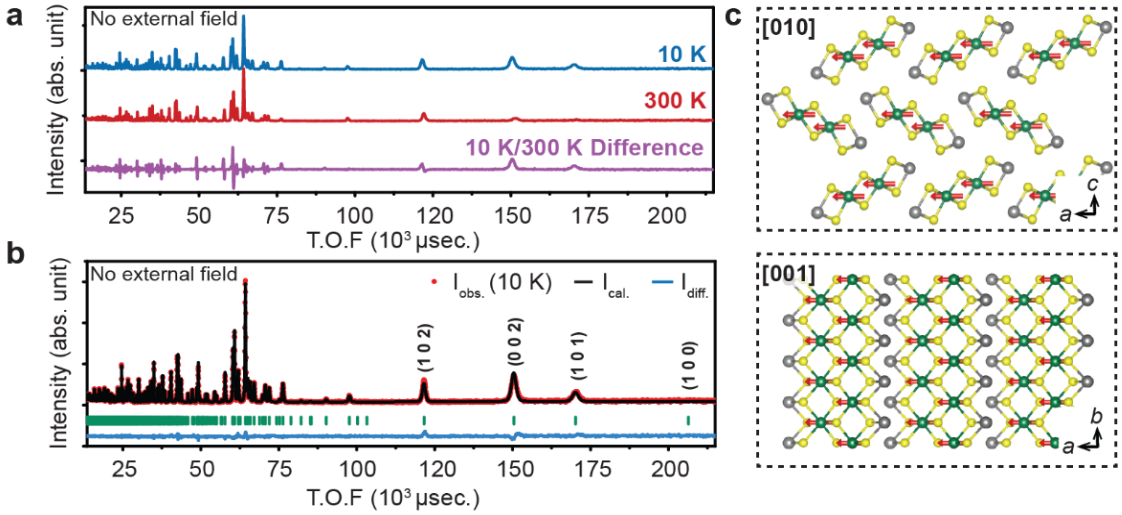

Figure 2. Magnetic structure of the $CrSbSe_3$ lattice. a) Comparison of the neutron diffraction profiles at 10 K (ferromagnetic state) and 300 K (paramagnetic state) in the absence of an external magnetic field. b) Final observed (red dots), fitted (black curve) and difference (blue curve) powder neutron diffractograms of bulk $CrSbSe_3$. Several zone axes of interest are labeled with their respective Miller indices. c) The refined magnetic structure of $CrSbSe_3$ derived from the powder neutron diffraction profile projected along the [010] (top) and [001] (bottom) axes.

refinement of the neutron diffraction patterns revealed ferromagnetic order with spin moments aligned along the *a* axis (**Figure 2c**). Because magnetic neutron scattering is sensitive only to the magnetic moment components that are perpendicular to the scattering vector, the absence of the magnetic (100) peak indicates perfect alignment of the ferromagnetically ordered moments along the *a* axis, without spin canting. These data confirm the magneto-crystalline anisotropy and the magnetic easy axis, previously suggested solely on the basis of magnetic susceptibility measurements of oriented crystals.[63] Similarly, the neutron diffraction-derived magnetic moment of 3.06(7) μ_B/Cr is consistent with the ground spin state of S = 3/2 for Cr(III), determined from magnetization data.

With evidence in hand that $CrSbSe_3$ presents as a quasi-1D vdW crystal that shows both magnetic ordering and significant anisotropy, we sought to investigate changes to these properties upon isolating nanowires from the bulk. To do so, we employed a solution technique pervasive in 2D vdW materials that involves systematic tuning of polarity and dispersity of solvent mixtures to optimize exfoliation.[67-70] To this end, the isopropanol (iPrOH)-water mixture covers a wide range of both dispersive and polar parameters and was also used here.[70-71] For $CrSbSe_3$, we found that a volumetric 30:70 *i*PrOH:water mixture yields the highest concentration of dispersed $CrSbSe_3$ nanowires (**Figure 3a, Table S5**). Although exfoliation of bulk $CrSbSe_3$ powder in 100% *i*PrOH also gives a somewhat even more concentrated dispersion, it leads to isotropic nanoparticles of $CrSbSe_3$ rather than nanowires (**Figure S4**). Subjecting the suspended $CrSbSe_3$ nanowires to liquid cascade centrifugation (See **Section I** in **Supporting Information** for exfoliation details) yields abundant nanowires with length exceeding 1 µm (**Figure 3b, S1**). Measurement of 70 individual randomly oriented nanowires using atomic force microscopy (AFM) gave an average cross-section of 10 ± 2.8 nm (**Figure 3c, S2**). Thus, the exfoliation-centrifugation method is particularly efficient at producing ultrathin and long wires with a narrow cross-sectional distribution. Indeed, three-dimensional AFM topographical view of single nanowires revealed uniform thickness along the length of the nanowire, with no tapering, branching, or kinking that are often seen in nanowires grown by bottom-up methods (**Figure 3d** bottom). Furthermore, nanowires produced by our method are smooth, with surface roughness of ± 0.2 nm over 1 µm, further highlighting the absence of morphological distortions, discontinuities, or cracks along the nanowire surface (**Figure S3**). This successful exfoliation process demonstrates that concepts and techniques in traditional top-down exfoliation in 2D vdW materials can be extended and translated to magnetic vdW materials with lower dimensionalities.

Raman spectroscopy and X-ray photoelectron spectroscopy (XPS) confirmed the phase identity, crystallinity, and surface stability of the exfoliated $CrSbSe_3$ nanowires. Because phonon modes are directly correlated to the structural identity and inherent crystallinity of a material, we probed the evolution of these modes in $CrSbSe_3$ upon its exfoliation from bulk into nanowires. As shown in **Figure 3e** (See also **Section 4** in **Supporting Information**), all Raman modes present in bulk $CrSbSe_3$ are also found in exfoliated nanowires, including the most prominent bands at 212.8 cm^{-1} and 174.4 cm^{-1}, whose

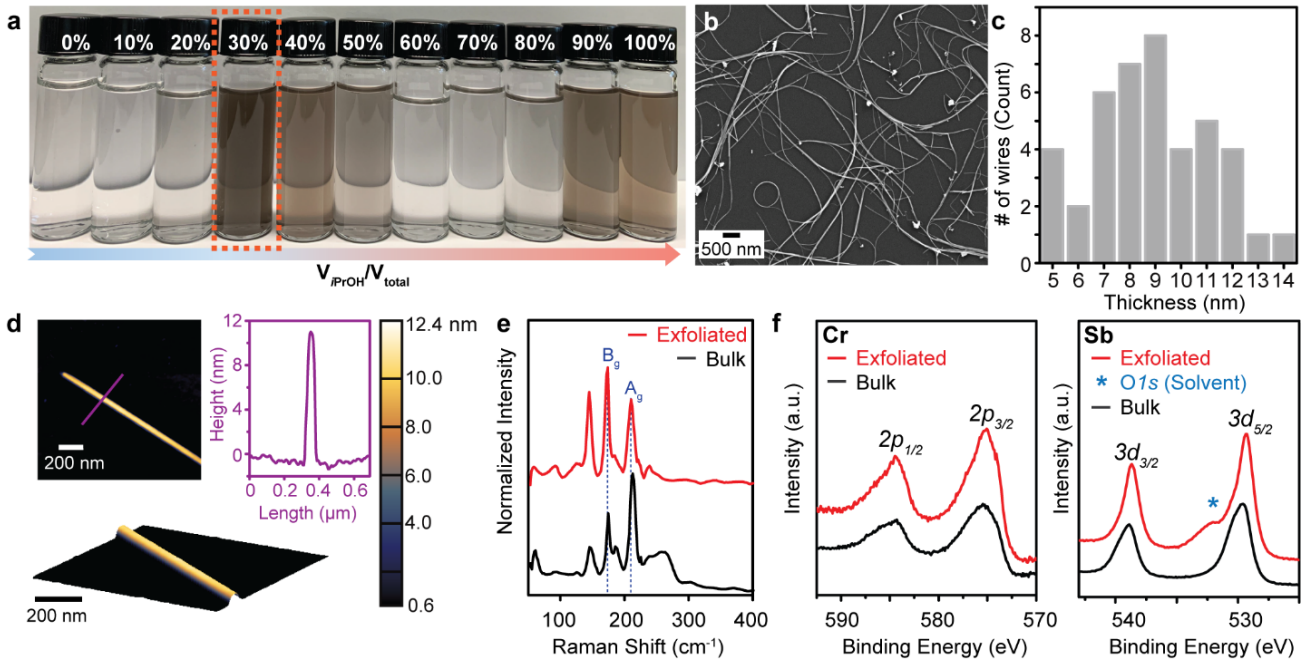

Figure 3. Morphology and stability of solution-exfoliated $CrSbSe_3$ nanowires. a) $CrSbSe_3$ dispersions in iPrOH/H_2O solvent mixtures with increasing *i*PrOH volume ratios (%V_{iPrOH}/V_{total}) and decreasing polarity from left to right. V_{total} denotes the total volume of *i*PrOH and H_2O. **b)** Representative SEM micrograph of the drop-casted $CrSbSe_3$ nanowires on 300 nm SiO_2/Si. **c)** Cross-section distributions of $CrSbSe_3$ nanowires determined by AFM imaging. **d)** AFM image of a single $CrSbSe_3$ nanowire with the corresponding line profile (top) and 3D topographical view (bottom). **e)** Micro-Raman spectra of the bulk and exfoliated $CrSbSe_3$. The symmetries of the phonon modes corresponding to directions perpendicular (A_g) and parallel (B_g) to the crystal long axis are labeled in blue and purple, respectively. **f)** XPS spectra of the Cr 2p and the Sb 3d of both bulk crystals and exfoliated nanowires of $CrSbSe_3$. In Sb 3d spectrum, the peak marked by an asterisk corresponds to the O 1s contribution from the exfoliation solvent.

narrow full-width half-max of 10.0 cm^{-1} and 6.3 cm^{-1}, respectively, remain nearly unchanged and indicate a high degree of crystallinity. We attribute lower energy shifts of approximately 2 cm^{-1} to phonon confinement effects as the lattice is reduced from bulk to nanowires.[72] XPS of $CrSbSe_3$ single crystals and exfoliated nanowires, shown in **Figure 3f**, revealed two energy bands for Cr, at 575.2 eV ($2p_{3/2}$) and 584.6 eV ($2p_{1/2}$), which agree well with the reported binding energy of Cr *2p* in similar coordination environments.[73] The broad non-symmetric peak shape of the Cr *2p* peaks can be attributed to multiplet splitting, which is common for Cr(III) compounds (See **Figure S6** for detailed peak fitting).[74] Similarly, the Sb *3d* spectra of bulk crystals and exfoliated nanowires both show two bands at 529.3 eV ($3d_{5/2}$) and 538.8 eV ($3d_{3/2}$), in good agreement with literature values for Sb (See **Figure S7** for detailed peak fitting).[75] Notably, there are no signs of oxidation upon exfoliation, as evidenced by the absence of higher binding energy peaks in both the Cr *2p* and the Sb *3d* regions (See Se *3d* region in **Figure S8**).

Exfoliating bulk crystals into nanowires allows systematic studies for understanding the evolution of magnetic properties of $CrSbSe_3$ upon nanosizing. We first confirmed the magnetic properties of bulk $CrSbSe_3$ by susceptibility measurements from 2 K to 300 K under an applied field of 1 kOe. A linear fit of this data in the high temperature region gives an effective moment of 4.2 μ_B/Cr, in agreement with the spin-only value expected for Cr(III) (3.9 μ_B). Fitting this data to the Curie-Weiss law gives θ_{CW} ~ 133 K, indicating ferromagnetic coupling between the Cr^{3+} centers, with T_C around 70 K (See fitting details in **Table S7**). The field-dependent magnetization curve at 2 K collected at fields up to 80 kOe saturates at 3 μ_B/Cr, further confirming both the phase purity and ferromagnetic ordering of the Cr^{3+} spins in the bulk $CrSbSe_3$ lattice (**Figure 4a**). Close inspection of the magnetic hysteresis loop indicates that both the coercivity, H_c, and the remanence are very low (H_c = 140 Oe), in agreement with previous reports classifying bulk $CrSbSe_3$ as a soft ferromagnet.[63-64]

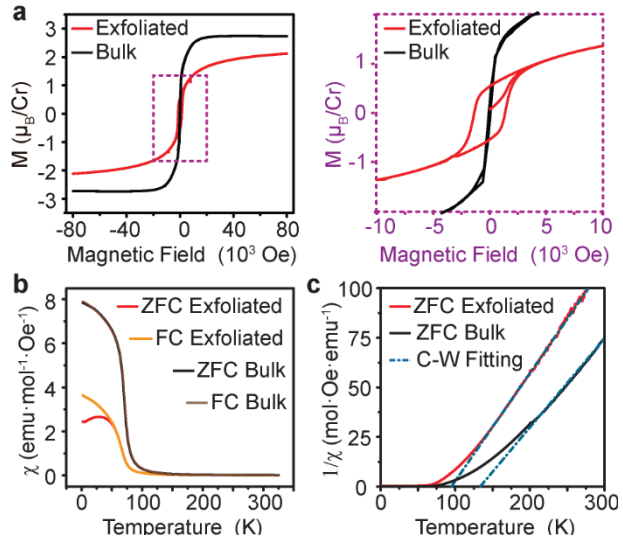

Figure 4. Magnetic properties of bulk polycrystalline powder and exfoliated nanowires of $CrSbSe_3$. a) Comparison of the M-H data for bulk and exfoliated nanowires of $CrSbSe_3$ at 2 K. (b) Temperature dependent field-cooled (FC) and zero field-cooled (ZFC) molar magnetic susceptibility curves of bulk and exfoliated $CrSbSe_3$ under an applied field of 1 kOe (c) Curie-Weiss fits of the temperature-dependent inverse susceptibilities for bulk and exfoliated $CrSbSe_3$.

Generally, the magnetization behavior of nanostructures tends to minimize the total free energy in terms of exchange energy, Zeeman energy, magnetoelastic energy, and anisotropy energy. Among these, the variation of the anisotropy term with particle shape has been experimentally and theoretically investigated extensively,[20, 76-77] and has been found to significantly influence fundamental magnetic properties including the coercivity, remanence, saturation magnetization, easy axis, and magnetic reversal process.[20, 77-78] Naturally, particle size also affects physical properties, especially when reaching the nanometer regime.[79] In magnetism, these finite-size effects are evident, for instance, when the particle size reaches that of the excitation wavelength of magnons, the domain wall width, or the spin-spin correlation length. Given the significantly altered morphology and particle size upon exfoliation, it is therefore reasonable to expect that nanowires of $CrSbSe_3$ should show different magnetic properties from the bulk.

Directly probing the magnetic properties of a single nanowire by magnetic force microscopy or magnetic-optical methods such as Kerr microscopy is challenging due to the low magnetic ordering temperature of $CrSbSe_3$ and the extreme thinness of the exfoliated nanowires that are well below the optical diffraction limit. An alternative method, demonstrated previously for exfoliated 2D hematite crystals, involves collecting the exfoliated particles and interpreting their collective magnetic properties.[66] Here, we filtered the final supernatant after the liquid cascade centrifugation and collected about 1 mg of exfoliated $CrSbSe_3$ nanowires. The shape of the magnetization curve for these nanowires (**Figure 4a**) suggests that the long-range ferromagnetic ordering present in bulk $CrSbSe_3$ persists upon exfoliation. However, the hysteresis loop demonstrates that the coercivity is significantly enhanced by as much as one order of magnitude, from H_c = 0.14 kOe in the bulk to H_c = 1.5 kOe in the exfoliated nanowires, and that the remanence increases from 0.2 μ_B/Cr in the bulk to 0.5 μ_B/Cr in the exfoliated nanowires. Notably, these results suggest that upon exfoliation into ultrathin nanowires, $CrSbSe_3$ transitions from a soft to a hard ferromagnet. Similar transitions have been observed for other low-dimensional magnetic systems and are often assigned to increasing anisotropy.[80-84] In bulk $CrSbSe_3$, although the spins prefer to align along the *a* axis, the magneto-crystalline anisotropy is relatively weak, as manifested by the low coercivity and low remanence. However, exfoliation into nanowires greatly changes the aspect ratio whereby the wire dimension along the crystallographic *b* direction is much longer than along *a* and *c*, giving rise to strong shape anisotropy. Consequently, the anisotropy energy increases, which imposes a greater barrier to spin flipping and induces a greater hysteresis.

Further understanding of the evolution of magnetic properties upon exfoliation came from analyzing the temperature-dependent magnetic susceptibility from 2 K to 300 K under an external field of 1 kOe. The zero-field cooled (ZFC) and field cooled (FC) magnetization curves bifurcate at low temperatures, consistent with the expected behavior of hard magnets (**Figure 4b**).85 The susceptibility data above 140 K can be fitted to the Curie-Weiss law to give a Curie constant of 3.9 μ_B/Cr and θ_{CW} of approximately 95 K. This θ_{CW} is 38 K lower than the value for the bulk crystal (**Figure 4c**, **Table S7**)

and can be ascribed to finite-size effects: in bulk $CrSbSe_3$, which is a 3D ferromagnet, the spin-spin correlation length $\boldsymbol{\xi}$ is expected to increase with temperature and diverge at the ordering temperature.[86] Upon exfoliation, where the dimensions along the crystallographic *a* and *c* directions become significantly smaller, the growth of the correlation length with temperature is constrained by the wire diameter ***d***, resulting in a reduced θ_{CW}. Although similar finite-size effects have been established both experimentally and theoretically in 2D thin films as well as zero-dimensional nanoparticles,[79, 87-90] they are much less investigated in 1D or quasi-1D nanowires, with several theoretical and experimental reports nevertheless showing strong size dependence of θ_{CW}.[91]

CONCLUSIONS

The foregoing results demonstrate that solution exfoliation is an efficient technique for accessing ultrathin ferromagnetic nanowires with high aspect ratio from bulk crystals of 1D vdW-connected lattices. As proof-of-principle, we showed that $CrSbSe_3$, a bulk ferromagnet made from vdW-connected 1D chains, serves as a good precursor for obtaining air-stable, free-standing nanowires that show increased coercivity and remanence compared to the bulk. These results provide a blueprint for additional studies with other bulk 1D vdW crystals. They further motivate studies aimed at understanding how magnetic interactions in bulk crystals evolve upon nanostructuring.

ASSOCIATED CONTENT

Supporting Information

Additional experimental details and characterization data. This material is available free of charge via the Internet at http://pubs.acs.org.

AUTHOR INFORMATION

Corresponding Author

*mdinca@mit.edu

Author Contributions

+These authors contributed equally.

Notes

The authors declare no competing financial interests.

ACKNOWLEDGMENT

The experimental work was supported by the Army Research Office (Award No. W911NF-21-1-0124). Neutron experiments used resources at the Spallation Neutron Source, a DOE Office of Science User Facility operated by the Oak Ridge National Laboratory. Part of the characterization was performed at the Harvard Center for Nanoscale Systems (CNS), a member of the National Nanotechnology Infrastructure Network (NNIN), which is supported by the National Science Foundation (Award No. ECS-0335765).

REFERENCES

(1) Dejongh, L. J.; Miedema, A. R., Experiments on Simple Magnetic Model Systems. *Adv. Phys.* **1974,** *23* (1), 1-260.

(2) Steiner, M.; Villain, J.; Windsor, C. G., Theoretical and Experimental Studies on One-Dimensional Magnetic Systems. *Adv. Phys.* **1976,** *25* (2), 87-209.

(3) Li, M. Y. M.; Claire, F. J.; Solomos, M. A.; Tenney, S. M.; Ivanov, S. A.; Siegler, M. A.; Kempa, T. J., Molecular Chains of Coordinated Dimolybdenum Isonicotinate Paddlewheel Clusters. *RSC Adv.* **2019,** *9* (29), 16492-16495.

(4) Bray, J. W.; Hart, H. R.; Interrante, L. V.; Jacobs, I. S.; Kasper, J. S.; Watkins, G. D.; Wee, S. H.; Bonner, J. C., Observation of a Spin-Peierls Transition in a Heisenberg Antiferromagnetic Linear-Chain System. *Phys. Rev. Lett.* **1975,** *35* (11), 744-747.

(5) Maekawa, S., Superconductivity in Spin Ladders. *Science* **1996,** *273* (5281), 1515-1515.

(6) Gschneidner, K. A.; Pecharsky, V. K.; Tsokol, A. O., Recent Developments in Magnetocaloric Materials. *Rep. Prog. Phys.* **2005,** *68* (6), 1479-1539.

(7) Gutfleisch, O.; Willard, M. A.; Bruck, E.; Chen, C. H.; Sankar, S. G.; Liu, J. P., Magnetic Materials and Devices for the 21st Century: Stronger, Lighter, and More Energy Efficient. *Adv. Mater.* **2011,** *23* (7), 821-842.

(8) Yuan, J. Y.; Xu, Y. Y.; Muller, A. H. E., One-dimensional Magnetic Inorganic-organic Hybrid Nanomaterials. *Chem. Soc. Rev.* **2011,** *40* (2), 640-655.

(9) Long, Y. Z.; Yu, M.; Sun, B.; Gu, C. Z.; Fan, Z. Y., Recent Advances in Large-scale Assembly of Semiconducting Inorganic Nanowires and Nanofibers for Electronics, Sensors and Photovoltaics. *Chem. Soc. Rev.* **2012,** *41* (12), 4560-4580.

(10) Caretta, L.; Mann, M.; Buttner, F.; Ueda, K.; Pfau, B.; Gunther, C. M.; Hessing, P.; Churikoval, A.; Klose, C.; Schneider, M.; Engel, D.; Marcus, C.; Bono, D.; Bagschik, K.; Eisebitt, S.; Beach, G. S. D., Fast Current-driven Domain Walls and Small Skyrmions in a Compensated Ferrimagnet. *Nat. Nanotechnol.* **2018,** *13* (12), 1154-1160.

(11) Sun, S. H.; Murray, C. B.; Weller, D.; Folks, L.; Moser, A., Monodisperse FePt Nanoparticles and Ferromagnetic FePt nanocrystal superlattices. *Science* **2000,** *287* (5460), 1989-1992.

(12) Allwood, D. A.; Xiong, G.; Faulkner, C. C.; Atkinson, D.; Petit, D.; Cowburn, R. P., Magnetic domain-wall logic. *Science* **2005,** *309* (5741), 1688-1692.

(13) Zhou, B. H.; Rinehart, J. D., A Size Threshold for Enhanced Magnetoresistance in Colloidally Prepared $CoFe_2O_4$ Nanoparticle Solids. *ACS Cent. Sci.* **2018,** *4* (9), 1222-1227.

(14) Zhou, B. H.; Rinehart, J. D., Pseudo Spin Valve Behavior in Colloidally Prepared Nanoparticle Films. *ACS. Appl. Electron. Mater.* **2019,** *1* (7), 1065-1069.

(15) Stano, M.; Fruchart, O.; Bruck, E., Chapter 3-Magnetic Nanowires and Nanotubes. In *Handbook of Magnetic Materials*, Elsevier: Amsterdam, **2018**; Vol. 27, pp 155-267.

(16) Dasgupta, N. P.; Sun, J. W.; Liu, C.; Brittman, S.; Andrews, S. C.; Lim, J.; Gao, H. W.; Yan, R. X.; Yang, P. D., 25th Anniversary Article: Semiconductor Nanowires Synthesis, Characterization, and Applications. *Adv. Mater.* **2014,** *26* (14), 2137-2184.

(17) Duan, X. F.; Lieber, C. M., General synthesis of compound semiconductor nanowires. *Adv. Mater.* **2000,** *12* (4), 298-302.

(18) Chowdhury, T.; Sadler, E. C.; Kempa, T. J., Progress and Prospects in Transition-Metal Dichalcogenide Research Beyond 2D. *Chem. Rev.* **2020,** *120* (22), 12563-12591.

(19) Cao, G. Z.; Liu, D. W., Template-based synthesis of nanorod, nanowire, and nanotube arrays. *Adv. Colloid. Interfac. Sci.* **2008,** *136* (1-2), 45-64.

(20) Sellmyer, D. J.; Zheng, M.; Skomski, R., Magnetism of Fe, Co and Ni nanowires in self-assembled arrays. *J. Phys.-Condens. Mat.* **2001,** *13* (25), R433-R460.

(21) Kohli, S.; McCurdy, P. R.; Johnson, D. C.; Das, J.; Prieto, A. L.; Rithner, C. D.; Fisher, E. R., Template-Assisted Chemical Vapor Deposited Spinel Ferrite Nanotubes. *J. Phys. Chem. C* **2010,** *114* (46), 19557-19561.

(22) Ross, C. A.; Smith, H. I.; Savas, T.; Schattenburg, M.; Farhoud, M.; Hwang, M.; Walsh, M.; Abraham, M. C.; Ram, R. J., Fabrication of patterned media for high density magnetic storage. *J. Vac. Sci. Technol. B* **1999,** *17* (6), 3168-3176.

(23) Gambardella, P.; Dallmeyer, A.; Maiti, K.; Malagoli, M. C.; Eberhardt, W.; Kern, K.; Carbone, C., Ferromagnetism in one-dimensional monatomic metal chains. *Nature* **2002,** *416* (6878), 301-304.

(24) Huang, F.; Kief, M. T.; Mankey, G. J.; Willis, R. F., Magnetism in the Few-Monolayers Limit - a Surface Magnetooptic Kerr-Effect Study of the Magnetic-Behavior of Ultrathin Films of Co, Ni, and Co-Ni Alloys on Cu(100) and Cu(111). *Phys. Rev. B* **1994,** *49* (6), 3962-3971.

(25) Kim, T.; Chamberlin, R. V.; Bird, J. P., Large Magnetoresistance of Nickel-Silicide Nanowires: Non-Equilibrium Heating of Magnetically-Coupled Dangling Bonds. *Nano Lett.* **2013,** *13* (3), 1106-1110.

(26) Seo, K.; Varadwaj, K. S. K.; Mohanty, P.; Lee, S.; Jo, Y.; Jung, M. H.; Kim, J.; Kim, B., Magnetic properties of single-crystalline CoSI nanowires. *Nano Lett.* **2007,** *7* (5), 1240-1245.

(27) Hung, S. W.; Wang, T. T. J.; Chu, L. W.; Chen, L. J., Orientation-Dependent Room-Temperature Ferromagnetism of FeSi Nanowires and Applications in Nonvolatile Memory Devices. *J. Phys. Chem. C* **2011,** *115* (31), 15592-15597.

(28) Tanase, M.; Silevitch, D. M.; Hultgren, A.; Bauer, L. A.; Searson, P. C.; Meyer, G. J.; Reich, D. H., Magnetic trapping and self-assembly of multicomponent nanowires. *J. Appl. Phys.* **2002,** *91* (10), 8549-8551.

(29) Jorritsma, J.; Mydosh, J. A., Temperature-dependent magnetic anisotropy in Ni nanowires. *J. Appl. Phys.* **1998,** *84* (2), 901-906.

(30) Topolovsek, P.; Gadermaier, C.; Vengust, D.; Strojnik, M.; Strle, J.; Mihailovic, D., Unlocking the Functional Properties in One-Dimensional MoSI Cluster Polymers by Doping and Photoinduced Charge Transfer. *Nano Lett.* **2015,** *15* (2), 813-818.

(31) Celic, N.; Pavlica, E.; Borovsak, M.; Strle, J.; Buh, J.; Zavasnik, J.; Bratina, G.; Denk, P.; Scharber, M.; Sariciftci, N. S.; Mihailovic, D., Factors determining large observed increases in power conversion efficiency of P3HT:PCBM solar cells embedded with $Mo_6S_{9-x}I_x$ nanowires. *Synthetic Met.* **2016,** *212*, 105-112.

(32) Chae, S.; Oh, S.; Choi, K. H.; Jeon, J.; Liu, Z. X.; Wang, C.; Lim, C.; Dong, X.; Woo, C.; Asghar, G.; Chang, J.; Nurunnabi, M.; Kang, J.; Song, S. Y.; Yu, H. K.; Choi, J. Y., Aqueous Dispersion of One-Dimensional van der Waals Material $Mo_6S_3I_6$ with the Charge Type of the Hydrophobic Dispersant Tail. *ACS Appl. Bio. Mater.* **2020,** *3* (7), 3992-3998.

(33) Lin, H.; Cheng, H. M.; Liu, L.; Zhu, Z. W.; Shao, Y. H.; Papakonstantinou, P.; Mihailovic, D.; Li, M. X., Thionin attached to a gold electrode modified with self-assembly of $Mo_6S_{9-X}I_X$ nanowires for amplified electrochemical detection of natural DNA. *Biosens. Bioelectron.* **2011,** *26* (5), 1866-1870.

(34) Pfister, D.; Schafer, K.; Ott, C.; Gerke, B.; Pottgen, R.; Janka, O.; Baumgartner, M.; Efimova, A.; Hohmann, A.; Schmidt, P.; Venkatachalam, S.; van Wullen, L.; Schurmann, U.; Kienle, L.; Duppel, V.; Parzinger, E.; Miller, B.; Becker, J.; Holleitner, A.; Weihrich, R.; Nilges, T., Inorganic Double Helices in Semiconducting SnIP. *Adv. Mater.* **2016,** *28* (44), 9783-9791.

(35) Chae, S.; Siddiqa, A. J.; Kim, B. J.; Oh, S.; Choi, K. H.; Lee, K. H.; Kim, H. Y.; Yu, H. K.; Choi, J. Y., Isolation of inorganic molecular chains from rod-like bulk V_2Se_9 crystal by liquid exfoliation. *RSC Adv.* **2018,** *8* (62), 35348-35352.

(36) Lee, W. G.; Sung, D.; Lee, J.; Chung, Y. K.; Kim, B. J.; Choi, K. H.; Lee, S. H.; Jeong, B. J.; Choi, J. Y.; Huh, J., Tuning the electronic properties of highly anisotropic 2D dangling-bond-free sheets from 1D V_2Se_9 chain structures. *Nanotechnology* **2021,** *32* (9), 095203.

(37) Ploscaru, M. I.; Kokalj, S. J.; Uplaznik, M.; Vengust, D.; Turk, D.; Mrzel, A.; Mihailovic, D., Mo6S9-xIx nanowire recognitive molecular-scale connectivity. *Nano Lett.* **2007,** *7* (6), 1445-1448.

(38) Vrbanic, D.; Pejovnik, S.; Mihailovic, D.; Kutnjak, Z., Electrical conductivity of $Mo_6S_3I_6$ and $Mo_6S_{4.5}I_{4.5}$ nanowires. *J. Eur. Ceram. Soc.* **2007,** *27* (2-3), 975-978.

(39) Andzane, J.; Prikulis, J.; Dvorsek, D.; Mihailovic, D.; Erts, D., Two-terminal nanoelectromechanical bistable switches based on molybdenum-sulfur-iodine molecular wire bundles. *Nanotechnology* **2010,** *21* (12), 125706.

(40) Uplaznik, M.; Bercic, B.; Remskar, M.; Mihailovic, D., Quantum charge transport in $Mo_6S_3I_6$ molecular wire circuits. *Phys. Rev. B* **2009,** *80* (8), 085402.

(41) Strle, J.; Vengust, D.; Mihailovic, D., Inorganic Molecular-Scale MoSI Nanowire-Gold Nanoparticle Networks Exhibit Self-Organized Critical Self-Assembly. *Nano Lett.* **2009,** *9* (3), 1091-1095.

(42) Chae, S.; Oh, S.; Choi, K. H.; Lee, J. W.; Jeon, J.; Liu, Z. X.; Wang, C.; Woo, C.; Shi, L. Y.; Kang, J.; Song, S. Y.; Kim, S. J.; Lee, J. H.; Yu, H. K.; Choi, J. Y., Aqueous dispersion of 1D van der Waals $Mo_6S_3I_6$ crystal using biocompatible tri-block copolymer. *Ceram. Int.* **2021,** *47* (9), 11935-11941.

(43) Lee, J. W.; Chae, S.; Oh, S.; Kim, S. H.; Choi, K. H.; Meeseepong, M.; Chang, J.; Kim, N.; Kim, Y. H.; Lee, N. E.; Lee, J. H.; Choi, J. Y., Single-Chain Atomic Crystals as Extracellular Matrix-Mimicking Material with Exceptional Biocompatibility and Bioactivity. *Nano Lett.* **2018,** *18* (12), 7619-7627.

(44) Itzhaik, Y.; Niitsoo, O.; Page, M.; Hodes, G., Sb_2S_3-Sensitized Nanoporous TiO_2 Solar Cells. *J. Phys. Chem. C* **2009,** *113* (11), 4254-4256.

(45) Majkic, A.; Gadermaier, C.; Celic, N.; Topolovsek, P.; Bratina, G.; Mihailovic, D., $Mo_6S_{9-x}I_x$ nanowires as additives for enhanced organic solar cell performance. *Sol. Energ. Mat. Sol. C* **2014,** *127*, 63-66.

(46) Webber, D. H.; Brutchey, R. L., Alkahest for V2VI3 Chalcogenides: Dissolution of Nine Bulk Semiconductors in a Diamine-Dithiol Solvent Mixture. *J. Am. Chem. Soc.* **2013,** *135* (42), 15722-15725.

(47) Webber, D. H.; Buckley, J. J.; Antunez, P. D.; Brutchey, R. L., Facile dissolution of selenium and tellurium in a thiol-amine solvent mixture under ambient conditions. *Chem. Sci.* **2014,** *5* (6), 2498-2502.

(48) Sayettat, J.; Bull, L. M.; Jobic, S.; Gabriel, J. C. P.; Fourmigue, M.; Batail, P.; Brec, R.; Inglebert, R. L.; Sourisseau, C., Behaviour of the one-dimensional, inorganic polymer $^{1\infty}[MPS_4]^-$ anions (M = Ni, Pd) in organic solutions. *J. Mater. Chem.* **1999,** *9* (1), 143-153.

(49) Tarascon, J. M.; Disalvo, F. J.; Chen, C. H.; Carroll, P. J.; Walsh, M.; Rupp, L., First Example of Monodispersed $(Mo_3Se_3)^{1\infty}$ Clusters. *J. Solid. State. Chem.* **1985,** *58* (3), 290-300.

(50) Gong, C.; Li, L.; Li, Z. L.; Ji, H. W.; Stern, A.; Xia, Y.; Cao, T.; Bao, W.; Wang, C. Z.; Wang, Y. A.; Qiu, Z. Q.; Cava, R. J.; Louie, S. G.; Xia, J.; Zhang, X., Discovery of intrinsic ferromagnetism in two-dimensional van der Waals crystals. *Nature* **2017,** *546* (7657), 265-269.

(51) Huang, B.; Clark, G.; Navarro-Moratalla, E.; Klein, D. R.; Cheng, R.; Seyler, K. L.; Zhong, D.; Schmidgall, E.; McGuire, M. A.; Cobden, D. H.; Yao, W.; Xiao, D.; Jarillo-Herrero, P.; Xu, X. D., Layer-dependent ferromagnetism in a van der Waals crystal down to the monolayer limit. *Nature* **2017,** *546* (7657), 270-273.

(52) Burch, K. S.; Mandrus, D.; Park, J. G., Magnetism in two-dimensional van der Waals materials. *Nature* **2018,** *563* (7729), 47-52.

(53) O'Hara, D. J.; Zhu, T. C.; Trout, A. H.; Ahmed, A. S.; Luo, Y. K.; Lee, C. H.; Brenner, M. R.; Rajan, S.; Gupta, J. A.; McComb, D. W.; Kawakami, R. K., Room Temperature Intrinsic Ferromagnetism in Epitaxial Manganese Selenide Films in the Monolayer Limit. *Nano Lett.* **2018,** *18* (5), 3125-3131.

(54) Bonilla, M.; Kolekar, S.; Ma, Y. J.; Diaz, H. C.; Kalappattil, V.; Das, R.; Eggers, T.; Gutierrez, H. R.; Phan, M. H.; Batzill, M., Strong room-temperature ferromagnetism in VSe_2 monolayers on van der Waals substrates. *Nat. Nanotechnol.* **2018,** *13* (4), 289-293.

(55) Lee, J. U.; Lee, S.; Ryoo, J. H.; Kang, S.; Kim, T. Y.; Kim, P.; Park, C. H.; Park, J. G.; Cheong, H., Ising-Type Magnetic Ordering in Atomically Thin $FePS_3$. *Nano Lett.* **2016,** *16* (12), 7433-7438.

(56) Song, X. Y.; Yuan, F.; Schoop, L. M., The properties and prospects of chemically exfoliated nanosheets for quantum materials in two dimensions. *Appl. Phys. Rev.* **2021,** *8* (1), 011312.

(57) Song, X. Y.; Cheng, G. M.; Weber, D.; Pielnhofer, F.; Lei, S. M.; Klemenz, S.; Yeh, Y. W.; Filsinger, K. A.; Arnold, C. B.; Yao, N.; Schoop, L. M., Soft Chemical Synthesis of H_xCrS_2: An Antiferromagnetic Material with Alternating Amorphous and Crystalline Layers. *J. Am. Chem. Soc.* **2019,** *141* (39), 15634-15640.

(58) Djieutedjeu, H.; Lopez, J. S.; Lu, R. M.; Buchanan, B.; Zhou, X. Y.; Chi, H.; Ranmohotti, K. G. S.; Uher, C.; Poudeu, P. F. P., Charge Disproportionation Triggers Bipolar Doping in $FeSb_{2-x}Sn_xSe_4$ Ferromagnetic Semiconductors, Enabling a Temperature-Induced Lifshitz Transition. *J. Am. Chem. Soc.* **2019,** *141* (23), 9249-9261.

(59) Djieutedjeu, H.; Poudeu, P. F. P.; Takas, N. J.; Makongo, J. P. A.; Rotaru, A.; Ranmohotti, K. G. S.; Anglin, C. J.; Spinu, L.; Wiley, J. B., Structural-Distortion-Driven Cooperative Magnetic and Semiconductor-to-Insulator Transitions in Ferromagnetic $FeSb_2Se_4$. *Angew. Chem. Int. Edit.* **2010,** *49* (51), 9977-9981.

(60) Djieutedjeu, H.; Makongo, J. P. A.; Rotaru, A.; Palasyuk, A.; Takas, N. J.; Zhou, X. Y.; Ranmohotti, K. G. S.; Spinu, L.; Uher, C.; Poudeu, P. F. P., Crystal Structure, Charge Transport, and Magnetic Properties of $MnSb_2Se_4$. *Eur. J. Inorg. Chem.* **2011,** (26), 3969-3977.

(61) Ranmohotti, K. G. S.; Djieutedjeu, H.; Poudeu, P. F. P., Chemical Manipulation of Magnetic Ordering in $Mn_{1-x}Sn_xBi_2Se_4$ Solid-Solutions. *J. Am. Chem. Soc.* **2012,** *134* (34), 14033-14042.

(62) Ranmohotti, K. G. S.; Djieutedjeu, H.; Lopez, J.; Page, A.; Haldolaarachchige, N.; Chi, H.; Sahoo, P.; Uher, C.; Young, D.; Poudeu, P. F. P., Coexistence of High-Tc Ferromagnetism and n-Type Electrical Conductivity in $FeBi_2Se_4$. *J. Am. Chem. Soc.* **2015,** *137* (12), 4274-4274.

(63) Kong, T.; Stolze, K.; Ni, D. R.; Kushwaha, S. K.; Cava, R. J., Anisotropic magnetic properties of the ferromagnetic semiconductor $CrSbSe_3$. *Phys. Rev. Mater.* **2018,** *2* (1), 014410.

(64) Odink, D. A.; Carteaux, V.; Payen, C.; Ouvrard, G., Synthesis and Structure of $CrSbSe_3$ - a Pseudo-One-Dimensional Ferromagnet. *Chem. Mater.* **1993,** *5* (2), 237-240.

(65) OBarr, R.; Schultz, S., Switching field studies of individual single domain Ni columns. *J. Appl. Phys.* **1997,** *81* (8), 5458-5460.

(66) Balan, A. P.; Radhakrishnan, S.; Woellner, C. F.; Sinha, S. K.; Deng, L. Z.; de los Reyes, C.; Rao, B. M.; Paulose, M.; Neupane, R.; Apte, A.; Kochat, V.; Vajtai, R.; Harutyunyan, A. R.; Chu, C. W.; Costin, G.; Galvao, D. S.; Marti, A. A.; van Aken, P. A.; Varghese, O. K.; Tiwary, C. S.; Iyer, A. M. M. R.; Ajayan, P. M., Exfoliation of a non-van der Waals material from iron ore hematite. *Nat. Nanotechnol.* **2018,** *13* (7), 602-609.

(67) Backes, C.; Higgins, T. M.; Kelly, A.; Boland, C.; Harvey, A.; Hanlon, D.; Coleman, J. N., Guidelines for Exfoliation, Characterization and Processing of Layered Materials Produced by Liquid Exfoliation. *Chem. Mater.* **2017,** *29* (1), 243-255.

(68) Shen, J. F.; He, Y. M.; Wu, J. J.; Gao, C. T.; Keyshar, K.; Zhang, X.; Yang, Y. C.; Ye, M. X.; Vajtai, R.; Lou, J.; Ajayan, P. M., Liquid Phase Exfoliation of Two-Dimensional Materials by Directly Probing and Matching Surface Tension Components. *Nano Lett.* **2015,** *15* (8), 5449-5454.

(69) Wang, M.; Xu, X. W.; Ge, Y. C.; Dong, P.; Baines, R.; Ajayan, P. M.; Ye, M. X.; Shen, J. F., Surface Tension Components Ratio: An Efficient Parameter for Direct Liquid Phase Exfoliation. *ACS Appl. Mater. Inter.* **2017,** *9* (10), 9168-9175.

(70) Halim, U.; Zheng, C. R.; Chen, Y.; Lin, Z.; Jiang, S.; Cheng, R.; Huang, Y.; Duan, X., A rational design of cosolvent exfoliation of layered materials by directly probing liquid-solid interaction. *Nat. Commun.* **2013,** *4*, 2213.

(71) Shen, J. F.; Wu, J. J.; Wang, M.; Dong, P.; Xu, J. X.; Li, X. G.; Zhang, X.; Yuan, J. H.; Wang, X. F.; Ye, M. X.; Vajtai, R.; Lou, J.; Ajayan, P. M., Surface Tension Components Based Selection of Cosolvents for Efficient Liquid Phase Exfoliation of 2D Materials. *Small* **2016,** *12* (20), 2741-2749.

(72) Jia, X.; Lin, Z.; Zhang, T.; Puthen-Veettil, B.; Yang, T.; Nomoto, K.; Ding, J.; Conibeer, G.; Perez-Wurfl, I., Accurate analysis of the size distribution and crystallinity of boron doped Si nanocrystals via Raman and PL spectra. *RSC Adv.* **2017,** *7* (54), 34244-34250.

(73) Ramaraj, S.; Mani, S.; Chen, S. M.; Palanisamy, S.; Velusamy, V.; Hall, J. M.; Chen, T. W.; Tseng, T. W., Hydrothermal Synthesis of Cr_2Se_3 Hexagons for Sensitive and Low-level Detection of 4-Nitrophenol in Water. *Sci. Rep.* **2018,** *8,* 4839.

(74) Biesinger, M. C.; Payne, B. P.; Grosvenor, A. P.; Lau, L. W. M.; Gerson, A. R.; Smart, R. S., Resolving surface chemical states in XPS analysis of first row transition metals, oxides and hydroxides: Cr, Mn, Fe, Co and Ni. *Appl. Surf. Sci.* **2011,** *257* (7), 2717-2730.

(75) Liu, X. S.; Chen, J.; Luo, M.; Leng, M. Y.; Xia, Z.; Zhou, Y.; Qin, S. K.; Xue, D. J.; Lv, L.; Huang, H.; Niu, D. M.; Tang, J., Thermal Evaporation and Characterization of Sb_2Se_3 Thin Film for Substrate Sb_2Se_3/CdS Solar Cells. *ACS Appl. Mater. Inter.* **2014,** *6* (13), 10687-10695.

(76) Park, B. C.; Kim, Y. K., Synthesis, microstructure, and physical properties of metallic barcode nanowires. *Met. Mater. Int.* **2017,** *23* (3), 413-425.

(77) Sun, L.; Hao, Y.; Chien, C. L.; Searson, P. C., Tuning the properties of magnetic nanowires. *IBM J. Res. Dev.* **2005,** *49* (1), 79-102.

(78) Pignard, S.; Goglio, G.; Radulescu, A.; Piraux, L.; Dubois, S.; Declemy, A.; Duvail, J. L., Study of the magnetization reversal in individual nickel nanowires. *J. Appl. Phys.* **2000,** *87* (2), 824-829.

(79) Zhang, R. J.; Willis, R. F., Thickness-dependent Curie temperatures of ultrathin magnetic films: Effect of the range of spin-spin interactions. *Phys. Rev. Lett.* **2001,** *86* (12), 2665-2668.

(80) Tan, C.; Lee, J.; Jung, S. G.; Park, T.; Albarakati, S.; Partridge, J.; Field, M. R.; McCulloch, D. G.; Wang, L.; Lee, C., Hard magnetic properties in nanoflake van der Waals Fe_3GeTe_2. *Nat. Commun.* **2018,** *9,* 1554.

(81) Londono-Calderon, C. L.; Moscoso-Londono, O.; Muraca, D.; Arzuza, L.; Carvalho, P.; Pirota, K. R.; Knobel, M.; Pampillo, L. G.; Martinez-Garcia, R., Synthesis and magnetic properties of cobalt-iron/cobalt-ferrite soft/hard magnetic core/shell nanowires. *Nanotechnology* **2017,** *28* (24), 245605.

(82) Schlorb, H.; Uhlemann, M.; Haehnel, V.; Iselt, D.; Gebert, A., Electrodeposition of Fe-based Magnetic Alloy Nanowires. *Z. Phys. Chem.* **2013,** *227* (8), 1071-1082.

(83) Yang, W.; Cui, C. X.; Sun, J. B.; Wang, B. L., Fabrication and magnetic properties of Fe_3Co_7 alloy nanowire arrays. *J. Mater. Sci.* **2010,** *45* (6), 1523-1527.

(84) Li, C. L.; Wu, Q.; Yue, M.; Xu, H. H.; Palaka, S.; Elkins, K.; Liu, J. P., Manipulation of morphology and magnetic properties in cobalt nanowires. *AIP Adv.* **2017,** *7* (5), 056422.

(85) Tejada, J.; Zhang, X. X.; Hernandez, J. M., Magnetic Viscosity and Hysteresis Phenomena. In *Magnetic Hysteresis in Novel Magnetic Materials;* Hadjipanayis, G. C., Eds.; Springer: Dordrecht, **1997**; Vol. 338, pp 221-232.

(86) Kardar, M., *Statistical Physics of Fields*. Cambridge University Press: 2012.

(87) Tang, Z. X.; Sorensen, C. M.; Klabunde, K. J.; Hadjipanayis, G. C., Size-Dependent Curie-Temperature in Nanoscale $MnFe_2O_4$ Particles. *Phys. Rev. Lett.* **1991,** *67* (25), 3602-3605.

(88) Koon, N. C.; Jonker, B. T.; Volkening, F. A.; Krebs, J. J.; Prinz, G. A., Direct Evidence for Perpendicular Spin Orientations and Enhanced Hyperfine Fields in Ultrathin Fe(100) Films on Ag(100). *Phys. Rev. Lett.* **1987,** *59* (21), 2463-2466.

(89) Childress, J. R.; Chien, C. L.; Jankowski, A. F., Magnetization, Curie-Temperature, and Magnetic-Anisotropy of Strained (111) Ni/Au Superlattices. *Phys. Rev. B* **1992,** *45* (6), 2855-2862.

(90) Li, Y.; Baberschke, K., Dimensional Crossover in Ultrathin Ni(111) Films on W(110). *Phys. Rev. Lett.* **1992,** *68* (8), 1208-1211.

(91) Lopez-Ruiz, R.; Magen, C.; Luis, F.; Bartolome, J., High temperature finite-size effects in the magnetic properties of Ni nanowires. *J. Appl. Phys.* **2012,** *112* (7) 073906.

Insert Table of Contents artwork here

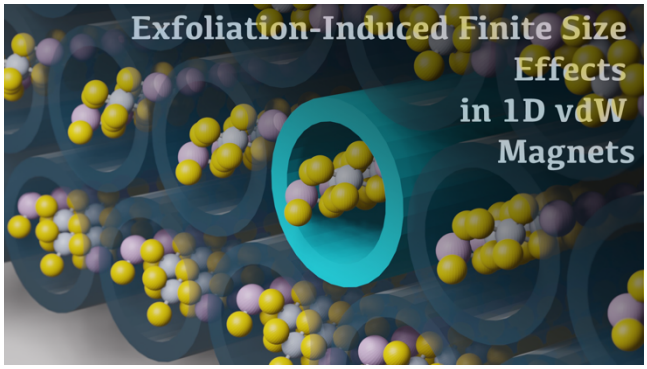

Supporting Information

Ultrathin, High-Aspect Ratio, and Free-Standing Magnetic Nanowires by Exfoliation of Ferromagnetic Quasi-One Dimensional van der Waals Lattices

Yi Qu,[a,+] Maxx Q. Arguilla,[a,+] Qiang Zhang,[b] Xin He,[a] and Mircea Dincă[a,*]

[a] Department of Chemistry, Massachusetts Institute of Technology, Cambridge, Massachusetts 02139, USA.

[b] Neutron Scattering Division, Oak Ridge National Laboratory, Oak Ridge, Tennessee 37831, USA

[+] Denotes equal contribution

*mdinca@mit.edu

Table of Contents

I. General procedures and experimental details

Synthesis of $CrSbSe_3$. Single crystals of $CrSbSe_3$, used in electron-dispersive X-ray spectroscopy (EDS) mapping, Raman spectroscopy and X-ray photoelectron spectroscopy (XPS), were grown *via* a modified high temperature flux method.[1] Elemental Cr, Sb, and Se were mixed in a molar ratio of Cr:Sb:Se = 7:33:60. Excess Sb and Se were used as flux, and the mixture was sealed into fused quartz tubes under a pressure of ~ 50 mTorr. The sealed ampoule was first ramped to 600 °C over 3 hours, kept at 600 °C for 3 hours, then ramped to 800 °C over 2 hours, and kept at this temperature for 3 days. The mixture was then cooled down to 680 °C slowly over 5 days and subsequently centrifuged at this temperature to remove the flux. The small amount of flux remaining on the surface of the crystals was removed by keeping the as-grown crystals at 500 °C for 3 days in a sealed fused quartz ampoule while leaving the cold end of the ampoule at room temperature. Polycrystalline powders of $CrSbSe_3$, used for time-of-flight (T.O.F.) powder neutron diffraction, magnetometry and exfoliation, were synthesized via a typical solid state melt reaction.[2] Starting elements were finely ground, mixed in stoichiometric ratio, and sealed into fused quartz tube under ~50 mTorr. Ampoules were heated to 800 °C over 3 hours and kept at this temperature for 2 days, followed by cooling to room temperature slowly over 5 days. The preparation and handling of all reagents was done under ambient conditions. Chromium (Sigma-Aldrich, 99.5%), antimony (STREM Chemicals, 99.5%) and selenium (STREM Chemicals, 99.99%) were purchased and used without further purification.

Liquid-phase exfoliation and liquid cascade centrifugation. Liquid-phase exfoliation was carried out *via* sonication (Branson 8800, 230 W, 25 °C) on finely ground samples dispersed in an isopropanol (*i*PrOH) and H_2O mixture with an optimized *i*PrOH volume fraction (V_{iPrOH} /V_{total}; V_{total} denotes the total volume of *i*PrOH and H_2O) and a starting concentration of 1 mg/mL for 2 hours. To eliminate large, unexfoliated solids, the resulting dispersion was first separated by centrifugation at 2000 r.p.m. for 10 minutes. The sediment from this centrifugation was removed and the supernatant was subjected to further centrifugation at 3000 r.p.m. for 5 minutes. This procedure was repeated at 4000 r.p.m. (3 minutes) and 5000 r.p.m. (3 minutes). Finally, the supernatant after centrifugation at 5000 r.p.m. was collected and used for subsequent measurements and characterization. The resulting supernatant was filtered under vacuum onto pre-weighed Millipore nitrocellulose filters with 25 nm pore size.

Characterization. The single crystal structure of $CrSbSe_3$ was confirmed *via* single crystal X-ray diffraction (SXRD) of sizeable micron-sized crystals using a Bruker D8 diffractometer which is coupled to a Bruker APEX-II CCD detector and a Mo Kα radiation (λ = 0.71073 Å), performing ϕ- and ω-scans. The refinement of the structure was performed using direct methods in the SHELX package and refined against F^2 on all data by full-matrix least squares with SHELXL-13.[3] The T.O.F. powder neutron diffraction data were collected on polycrystalline samples loaded into thin-walled vanadium cans, on the T.O.F. powder diffractometer POWGEN at the Spallation Neutron Source, Oak Ridge National Laboratory. Structural and magnetic refinements were performed using the FullProf package.[4] The symmetry-allowed magnetic

structures were derived using SARAH representational analysis program.[5] Magnetic susceptibility measurements were performed on powders using a Quantum Design Physical Property Measurement System (PPMS) Dynacool, equipped with a vibrating sample magnetometer (VSM) option. The polarized and unpolarized Raman spectra were collected on a Horiba Multiline Raman spectrometer with a 100x long working distance objective, 532 nm excitation line, and 600 gr/mm grating with a spot size of ~3 μm. The X-ray photoelectron spectra (XPS) were collected using a Thermo Nexsa X-ray photoelectron spectrometer with a monochromated Al X-ray source. Scanning electron microscopy (SEM) micrographs were acquired using a Zeiss Field Emission SEM Ultra55 equipped with an electron-dispersive X-ray spectroscopy (EDS) detector. Atomic force microscopy (AFM) images were acquired on a Cypher Atomic Force Microscope from Asylum Research using silicon probing tips with mid-range mechanical properties (f = 300 kHz, k = 26 N/m) from Oxford Instruments. The scan rates are 0.5-2 Hz depending on the scan size.

II. Crystal structure and magnetic structure details of bulk $CrSbSe_3$

Table S1. Details of the structure determination of $CrSbSe_3$ based on single-crystal experiments measured at 300 K

Sum Formula	$CrSbSe_3$
Radiation	λ (Mo-$K\alpha$ = 0.71073 Å)
Thera range for data collection	$2\theta \leq 61.004°$
Index ranges	$-13 \leq h \leq 13$, $-5 \leq k \leq 5$, $-19 \leq l \leq 19$
Absorption coefficient /mm^{-1}	31.590
Measured reflections	11064
Independent reflections	805
No. of parameters	31
Goodness-of-fit on F^2	1.218
Final R indices [$I > 2\sigma(I)$]	0.0716
R(int)	0.0564
$R(\sigma)$	0.0255
R indices (all data)	0.0720
ωR_2 (all data)	0.1662
Largest diff. peak and hole (e^-/ $Å^3$)	3.651 to -3.729

Table S2. Selected crystallographic data of $CrSbSe_3$ derived from Single-crystal X-ray Diffraction (SXRD) measured at 298 K, Time-of-Flight Powder Neutron Diffraction (T.O.F. PND) measured at 300 K and measured at 10 K.

	SXRD at 298 K	T.O.F. PND at 300 K	T.O.F. PND at 10 K
Crystal system	Orthorhombic	Orthorhombic	Orthorhombic
Space group	P n m a	P n m a	P n m a
Lattice parameter (Å)			
a	9.1552(3)	9.14356(14)	9.15077
b	3.78460(10)	3.78477 (5)	3.78376
c	13.3542(4)	13.41741(19)	13.33229
Cell volume ($Å^3$)	462.56(2)	464.326	461.621

Table S3. Atomic coordinates for $CrSbSe_3$ derived from SXRD at 298 K, T.O.F. PND measured at 300 K and 10 K.

	SXRD at 298 K		
Atom	***x***	***y***	***z***
Cr	0.34320(14)	0.2500	0.45537(10)
Sb	0.02882(6)	0.7500	0.34153(5)
Se(1)	0.17119(9)	-0.2500	0.51586(6)
Se(2)	0.49948(9)	0.2500	0.60836(7)
Se(3)	0.21424(9)	0.2500	0.28611(6)

	T.O.F. PND at 300 K			T.O.F. PND at 10 K		
Atom	***x***	***y***	***z***	***x***	***y***	***z***
Cr	0.15627(41)	0.25000(0)	0.04489(25)	0.15685(0)	0.25000(0)	0.04389(0)
Sb	0.02998(22)	0.25000(0)	0.65809(16)	0.02884(0)	0.25000(0)	0.65849(0)
Se(1)	0.17189(17)	0.25000(0)	0.48436(10)	0.17114(0)	0.25000(0)	0.48403(0)
Se(2)	0.50221(17)	0.25000(0)	0.60906(11)	0.50076(0)	0.25000(0)	0.60823(0)
Se(3)	0.28510(15)	0.25000(0)	0.21295(11)	0.28586(0)	0.25000(0)	0.21392(0)

Table S4. Selected bond lengths (or interatomic distances) of the refined CrSbSe3 structure derived from SXRD at 300 K.

	d (Å)
Cr-Se(1)	2.5907(11)
Cr-Se(2)	2.5255(11)
Cr-Se(3)	2.5499(16)
Sb-Se(1) (intra-chain covalent bond)	2.6679(11)
Sb-Se(3) (intra-chain covalent bond)	2.6473(8)
Sb-Se(1) (inter-chain vdW interaction)	3.2494(9)
Sb-Se(3) (inter-chain vdW interaction)	3.8439(9)

III. Exfoliation results of $CrSbSe_3$

Table S5. Concentrations of the $CrSbSe_3$ nanowire dispersions in isopropanol (*i*PrOH)/H_2O cosolvent system.

V_{iPrOH}/V_{total}	Concentration (mg/mL)
30%	0.043
40%	0.033
50%	0.031
90%	0.025
100%	0.025

Note: The concentrations of dispersions with other iPrOH percentages are too low to be measured accurately.

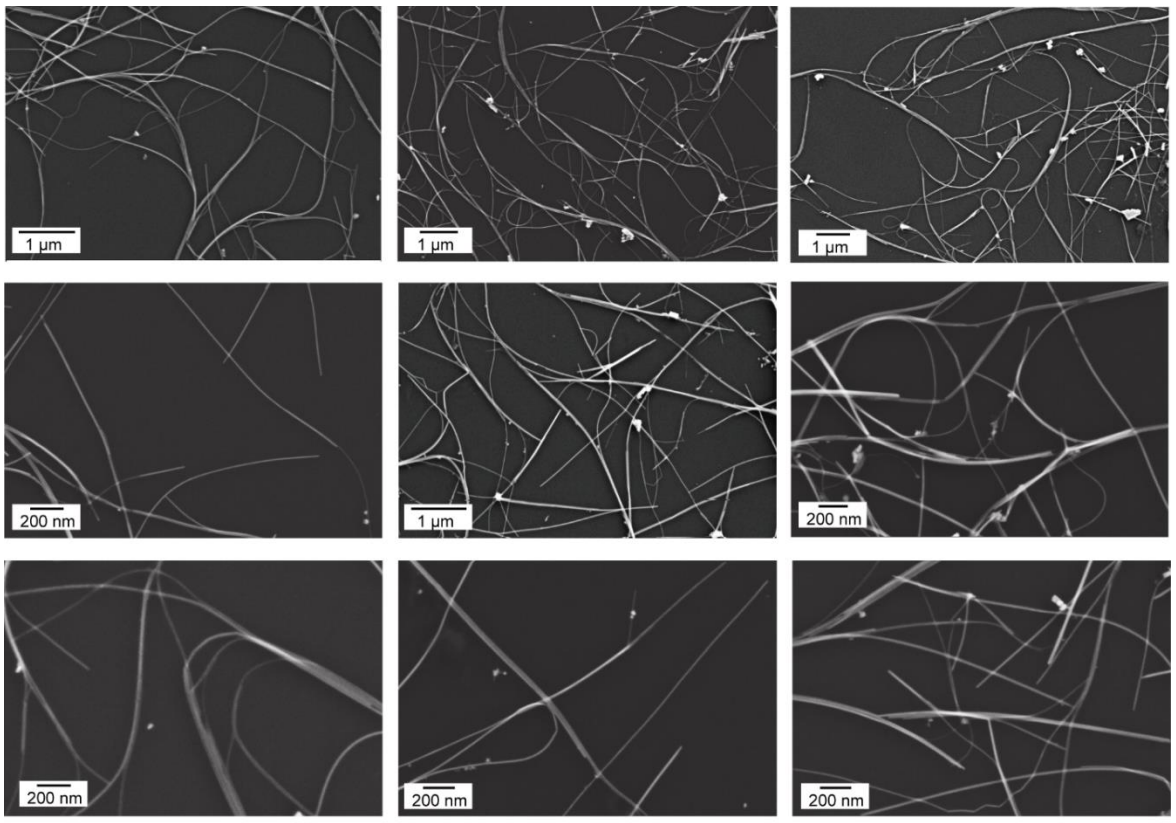

Figure S1. Representative SEM micrographs of the drop-casted $CrSbSe_3$ nanowires on 300 nm SiO_2/Si substrate.

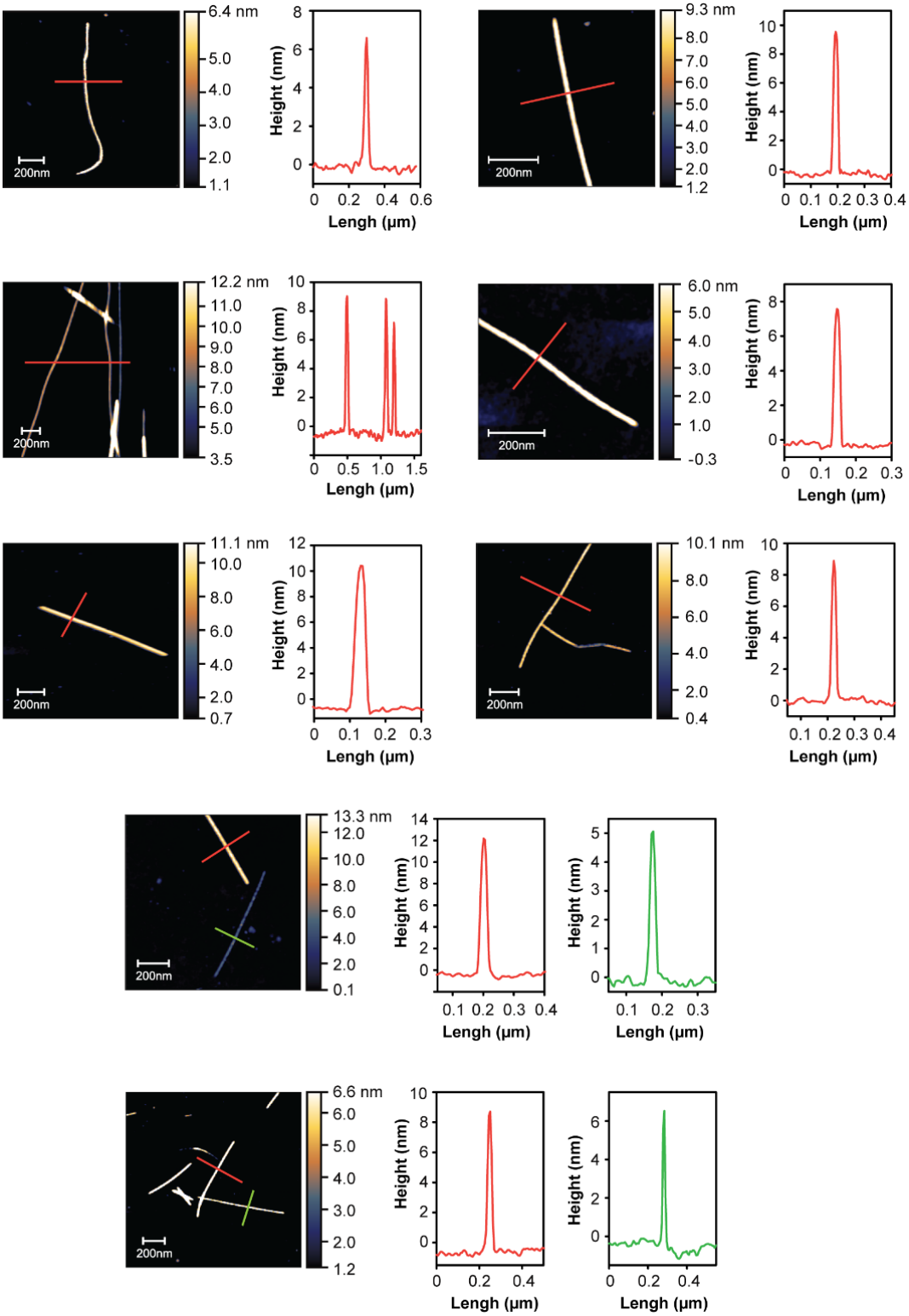

Figure S2. Representative AFM images and the corresponding height profiles of the exfoliated $CrSbSe_3$ nanowires.

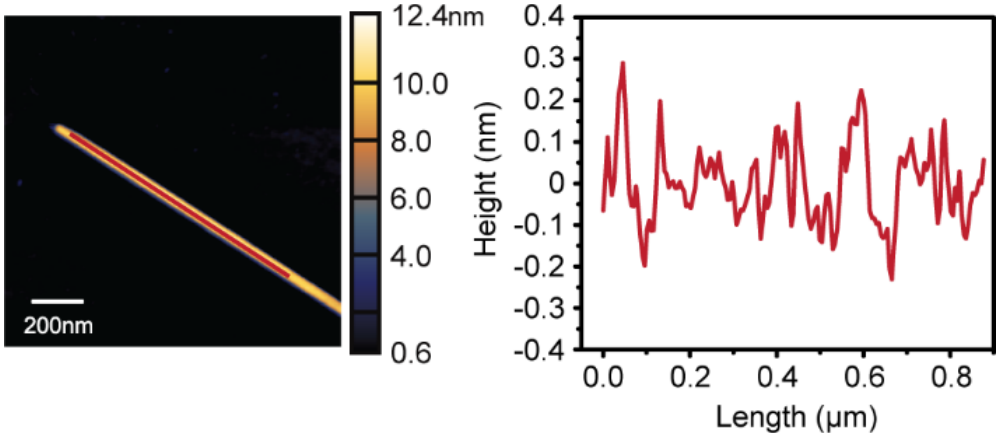

Figure S3. Surface roughness of one CrSbSe3 nanowire on 300nm SiO2/Si substrate.

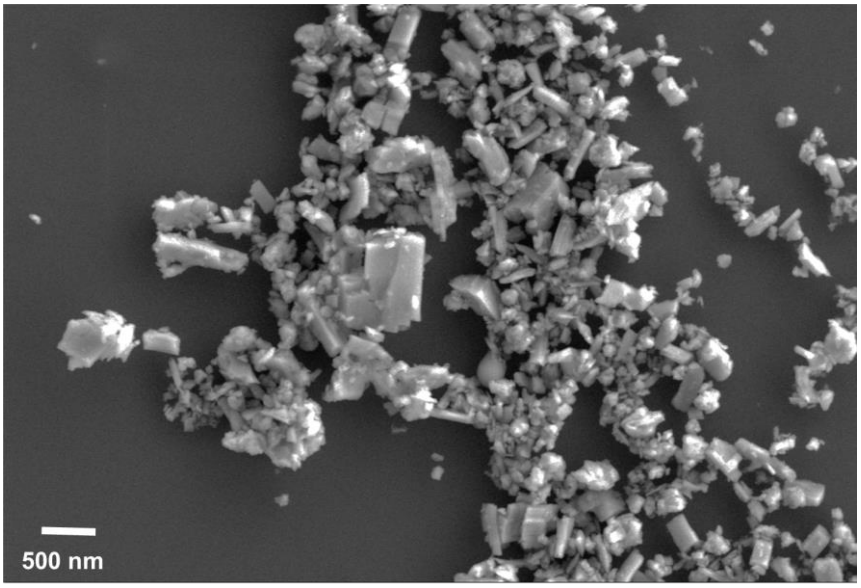

Figure S4. Representative SEM micrograph of the drop-casted exfoliated $CrSbSe_3$ nanoparticles in 100% *i*PrOH.

IV. Symmetry analysis of bulk $CrSbSe_3$ single crystal for Raman spectroscopy

We performed polarized Raman measurements in the backscattering geometry in order to probe the phonon modes in the $CrSbSe_3$ lattice. In these measurements, we performed (0^o) co- and (90^o) cross-polarized scattering measurements where the long axis of the crystal is parallel to the laser polarization. We used the standardized unit cell axes ($a \rightarrow a$, $b \rightarrow c$, $c \rightarrow b$), mainly assigning

the high-symmetry principal axis from *b* to *c*, instead of the experimental single crystal unit cell and reported unit cell axes [1-2] for coherence and consistency with the group theory analyses. This measurement setup corresponds to the –X(ZZ)X and –X(YZ)X Porto notations for the co- and cross-polarized measurements. Since we are doing only the crystal axes perpendicular to the crystal long axis, in this case, X and Y are interchangeable. This won't affect any of the subsequent selection rules due to the nature of the symmetry. Similar to other orthorhombic crystals that are comprised of isolated chains, with the same Pnma space group symmetry [6], we adopted the simplified C_{2h} point group instead of the D_{2h} point group. By doing this, we simplify and reduce the Raman-active modes from 30 modes ($2A_g + B_{1g} + 2B_{2g} + B_{3g}$ for 5 atoms occupying the 4c site) to 15 modes in total ($2A_g + B_{1g}$ for 5 atoms occupying the 4c site). In these modes, B_{1g} and A_g modes correspond to the vibrations parallel and perpendicular to the crystal's long axis. We experimentally observe 10 major peak modes of these 15 expected modes. Upon performing co-polarized measurements, we observe the persistence of only five peaks. These vibrational modes should therefore correspond to the A_g (vibrations perpendicular to the chain direction) symmetry based on Raman polarization selection rules. On the other hand, in the cross-polarized spectra, the five peaks that decreased in intensity and disappeared are the only ones that were present, thereby establishing the vibrational modes corresponding to these Raman shifts to be in the B_{1g} (vibrations parallel to the chain direction) symmetry.

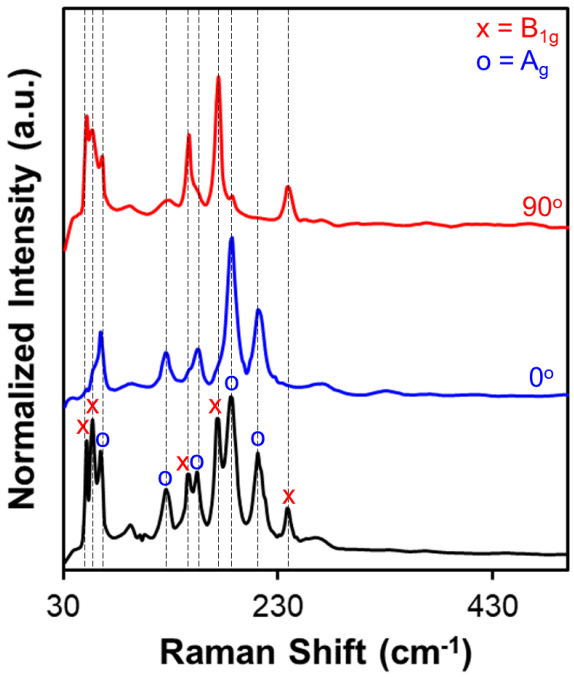

Figure S5. Unpolarized, co-polarized, and cross-polarized backscattered Raman spectra of CrSbSe3 single crystal with the symmetry assigned. (A_g: vibrations parallel to the wire direction; B_g: vibrations perpendicular to the wire direction)

Table S6. Fitting results of major Raman peaks of bulk and exfoliated $CrSbSe_3$.

	Bulk single crystal				Exfoliated nanowires			
Peak position (cm^{-1})	147.2	174.4	186.4	212.8	145.2	172.6	184.5	210.3
FWHM (cm^{-1})	9.86	6.32	13.05	10.05	8.23	7.07	10.48	10.67
Symmetry mode	A_g+B_g	B_g	A_g	A_g	A_g+B_g	B_g	A_g	A_g

V. Air-stability of exfoliated $CrSbSe_3$ nanowires

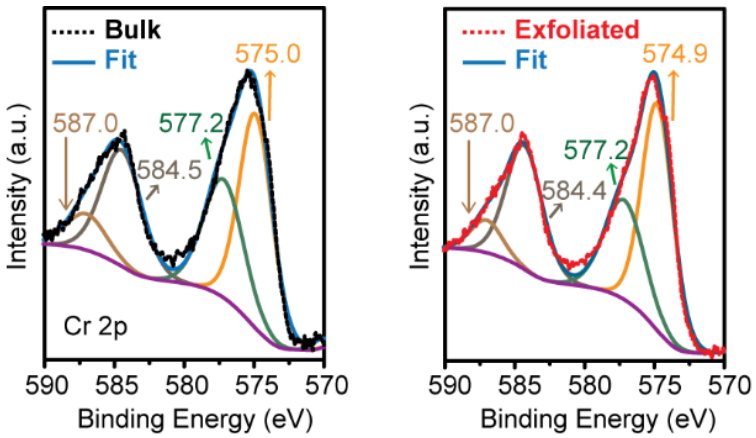

Figure S6. Fitting of the Cr *2p* XPS spectra of bulk and exfoliated $CrSbSe_3$.

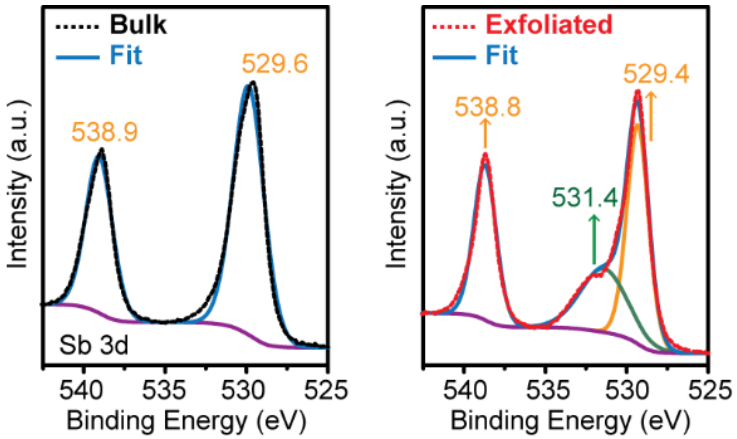

Figure S7. Fitting of the Sb *3d* XPS spectra of bulk and exfoliated $CrSbSe_3$.

The Sb $3d_{3/2}$ region of the exfoliated nanowires shows a miniscule shoulder at 532.0 eV which we ascribe to the O*1s* peak of the residual solvent.

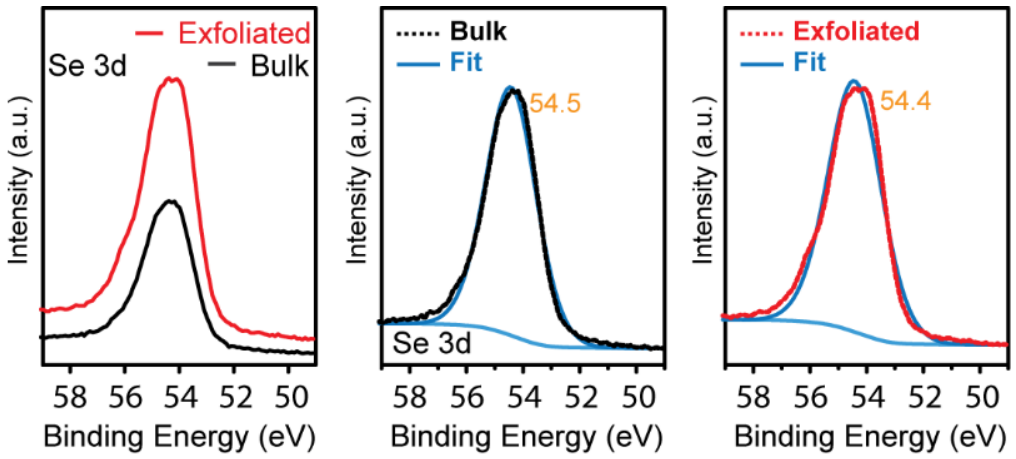

Figure S8. XPS spectrum of the Se 3d region of $CrSbSe_3$ before and after exfoliation (left) and the corresponding peak fitting (right).

VI. Magnetic properties of bulk and exfoliated $CrSbSe_3$

The inverse susceptibility ($1/\chi$) data gathered at low applied field (1000 Oe) were fitted using the modified Curie-Weiss law ($1/\chi = (T-\theta_{cw})/C$). The fitting parameters are shown in **Table S7.**

Table S7. Parameters derived from the Curie-Weiss fitting of bulk and exfoliated $CrSbSe_3$.

	Bulk	Exfoliated
Slope	0.4479	0.5436
Intercept	-59.7698	-51.5435
R^2	0.997	0.999
C	2.2326	1.8396
μ_{eff} (μ_B)	4.23	3.84
θ_{cw} (K)	133.4	94.8

References

1. Kong, T.; Stolze, K.; Ni, D. R.; Kushwaha, S. K.; Cava, R. J., Anisotropic magnetic properties of the ferromagnetic semiconductor $CrSbSe_3$. *Phys. Rev. Mater.* **2018,** *2* (1).
2. Odink, D. A.; Carteaux, V.; Payen, C.; Ouvrard, G., Synthesis and Structure of $CrSbSe_3$ - a Pseudo-One-Dimensional Ferromagnet. *Chem. Mater.* **1993,** *5* (2), 237-240.
3. Sheldrick, G. M., Crystal structure refinement with SHELXL. *Acta. Crystallogr. C: Struct. Chem.* **2015,** *71* (Pt 1), 3-8.
4. Rodríguez-Carvajal, J., Recent advances in magnetic structure determination by neutron powder diffraction. *Phys. Rev. B: Condens. Mat.* **1993,** *192*, 55-69.
5. Wills, A. S., A new protocol for the determination of magnetic structures using simulated annealing and representational analysis (SARAh). *Physica B* **2000,** *276*, 680-681.

6. Perry, C. H.; Agrawal, D. K., Raman Spectrum of Ferroelectric SbSI. *Solid State Commun.* **1970,** *8* (4), 225-230.